

# Laboratory Modelling of Sill Emplacement: Part 1 - saucer-shaped intrusions

Uchitha Suranga Nissanka Arachchige<sup>1</sup>, Alexander Cruden<sup>1</sup>, Roberto F. Weinberg<sup>1</sup>, Anja Slim<sup>1</sup>, and Jonas Köpping<sup>1</sup>

<sup>1</sup>Monash University

November 24, 2022

## Abstract

We investigate the conditions under which saucer-shaped sills form through the upper crust and their geometries. We performed a series of scaled laboratory experiments that employ visco-elastic-plastic Laponite RD<sup>®</sup> (LRD) gels to model upper crustal rocks, and Newtonian paraffin oil as the magma analogue. Both homogenous and layered analogue upper crust is considered. In homogenous 3 wt. % LRD, the injected oil formed a saucer-shaped intrusion with the shortest inner sill observed among all of the experiments. Saucer-shaped sills always formed in experiments with a two-layer upper crust. These experiments show sharp transitions from an inner flat sill to outer inclined sheets, which are characterised by non-planar margins. The experimental results show that: (1) the transition from an inner flat sill to outer inclined sheet occurs when the sill radius to overburden depth ratio ( $r/H$ ) is between 0.5 and 2.5; (2) the inclined sheets propagate upwards with angles,  $\theta = 15^\circ$  to  $25^\circ$ ; (3) the ratio of the Young's modulus ( $E^*$ ) between the layers controls when the inner flat sill to outer inclined sheet occurs; and (4) irregular finger-like and/or lobe segment geometries form at the propagating tip of the intrusion. The results also suggest that there is no strict requirement for high horizontal stresses to form natural saucer-shaped sill geometries. We conclude that the layered visco-elastic-plastic crustal analogues better represent natural, complex saucer-shaped sill geometries. Furthermore, the observed sharp transitions between inner and outer sills are compatible with brittle-elastic fracture mechanisms operating at the intrusion scale.

1 **Laboratory Modelling of Sill Emplacement: Part 1 – saucer-**  
2 **shaped intrusions**

3

4 Uchitha N. Arachchige<sup>1</sup>, Alexander R. Cruden<sup>1</sup>, Roberto Weinberg<sup>1</sup>, Anja Slim<sup>1</sup>, Jonas  
5 Köpping<sup>1</sup>

6

7 <sup>1</sup>School of Earth, Atmosphere and Environment, Monash University, 9 Rainforest Walk, Clayton, VIC 3800,  
8 Australia

9

10

11

12

13

14

15

16

17

18

19

20

## 21 **Abstract**

22 We investigate the conditions under which saucer-shaped sills form through the upper crust  
23 and their geometries. We performed a series of scaled laboratory experiments that employ  
24 visco-elastic-plastic Laponite RD® (LRD) gels to model upper crustal rocks, and Newtonian  
25 paraffin oil as the magma analogue. Both homogenous and layered analogue upper crust is  
26 considered. In homogenous 3 wt. % LRD, the injected oil formed a saucer-shaped intrusion  
27 with the shortest inner sill observed among all of the experiments. Saucer-shaped sills always  
28 formed in experiments with a two-layer upper crust. These experiments show sharp transitions  
29 from an inner flat sill to outer inclined sheets, which are characterised by non-planar margins.  
30 The experimental results show that: (1) the transition from an inner flat sill to outer inclined  
31 sheet occurs when the sill radius to overburden depth ratio ( $r/H$ ) is between 0.5 and 2.5; (2) the  
32 inclined sheets propagate upwards with angles,  $\theta = 15^\circ$  to  $25^\circ$ ; (3) the ratio of the Young's  
33 modulus ( $E^*$ ) between the layers controls when the inner flat sill to outer inclined sheet occurs;  
34 and (4) irregular finger-like and/or lobe segment geometries form at the propagating tip of the  
35 intrusion. The results also suggest that there is no strict requirement for high horizontal stresses  
36 to form natural saucer-shaped sill geometries. We conclude that the layered visco-elastic-  
37 plastic crustal analogues better represent natural, complex saucer-shaped sill geometries.  
38 Furthermore, the observed sharp transitions between inner and outer sills are compatible with  
39 brittle-elastic fracture mechanisms operating at the intrusion scale.

## 40 **Plain language summary**

41 When magma rise through the Earth's crust to the surface, it forms cracks within rock layers,  
42 which propagate upwards with the magma inside. These cracks often form "saucer-shaped sill"  
43 structures which transport magma horizontally and vertically within its inner flat and outer  
44 inclined regions, respectively. In order to understand how these saucer-shaped sills form and  
45 propagate within rock layers, we model them with experimental methods using similar

46 conditions to the nature and analyse the results of the experiments. In our experiments,  
47 Laponite RD® and paraffin oil represent the host rock and the ascending magma, respectively.  
48 We find that the saucer-shaped sills consist of sharp transitions from inner flat to outer inclined  
49 regions. Moreover, the leading edges of these cracks are irregular, which consists of finger and  
50 lobe shaped margins. Results suggest that the material properties of Laponite RD® better  
51 represent the natural rock behaviour and produce much similar saucer-shaped sills that of in  
52 nature. However, the experimental sills are more complex than previously modelled and future  
53 planning efforts should take these results into account.

54

55

56

57

58

59

60

61

62

63

64

65

66

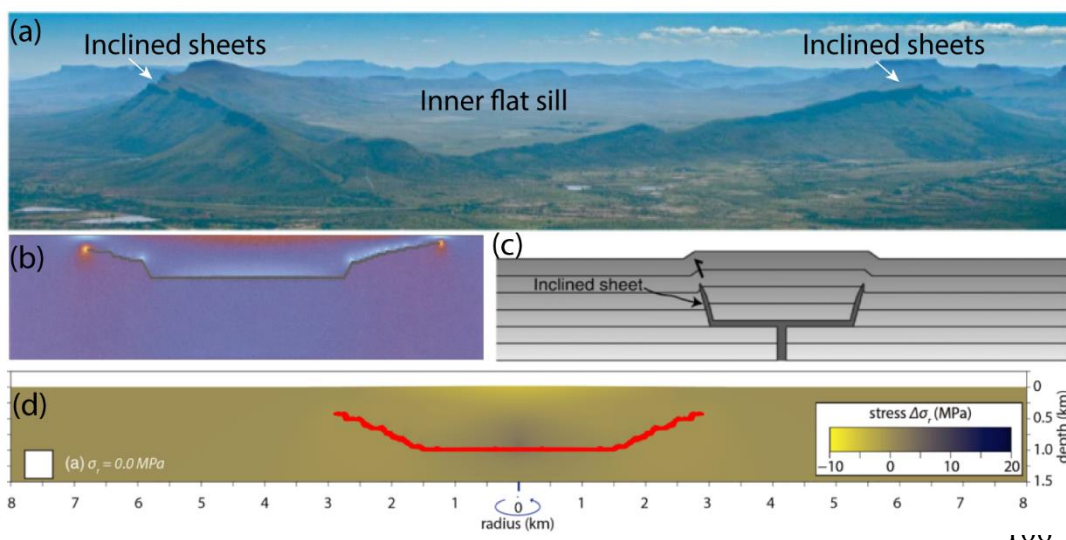
## 67 **1. Introduction**

68           Igneous sheet intrusions such as dykes and sills are broadly planar structures that are  
69 the principal pathways for the migration of magma through the upper crust. Although dykes  
70 have traditionally been considered to play the dominant role in magma plumbing systems,  
71 recent three dimensional (3D) seismic reflection studies of offshore sedimentary basins suggest  
72 that mafic sill complexes play a major, and perhaps leading, role in the vertical and horizontal  
73 transport of magma in the shallow crust (Magee et al., 2016; Eide et al., 2017). Such sill  
74 complexes often comprise non-planar, interconnected saucer-shaped sills and inclined, strata-  
75 discordant intrusions (Thomson and Hutton, 2004; Hansen and Cartwright, 2006).

76           Saucer-shaped sill morphologies are regarded to be a fundamental feature of mafic  
77 intrusions in shallow sedimentary basins (Galland et al., 2009; Galland & Scheibert, 2013;  
78 Chen et al., 2017). Field observations (e.g., Golden Valley Sill Complex, South Africa;  
79 Chevallier and Woodford, 1999; Planke et al., 2005; Planke, 2008) and two-dimensional (2D)  
80 and 3D seismic reflection observations (Hansen et al., 2004; Thomson and Hutton, 2004;  
81 Hansen and Cartwright, 2006; Hansen et al., 2008) of saucer-shaped sills indicate that they  
82 comprise a sub-horizontal, strata-concordant, inner sill, forming the base, and an inclined,  
83 strata-discordant, concave upward outer section (Figs. 1a, 2a). Field observations and 3D  
84 seismic surveys have also found that these intrusions can have non-planar, segmented outer  
85 margins consisting of lobes and fingers that range in scale from metres to kilometres (Pollard  
86 et al., 1975; Thomson and Hutton, 2004; Hansen and Cartwright, 2006; Magee et al., 2016).

87           The emplacement mechanisms of saucer-shaped sills are mainly attributed to either the  
88 elastic or plastic properties of the host rocks, as well as interaction with Earth's free surface.  
89 By considering the Mode I and Mode II stress intensity factors at the tip of a horizontal fluid-  
90 filled fracture in an elastic medium with a free upper surface, Pollard and Holzhausen (1978)  
91 showed that horizontal sills transition into inclined sheets when their depth is less than two-

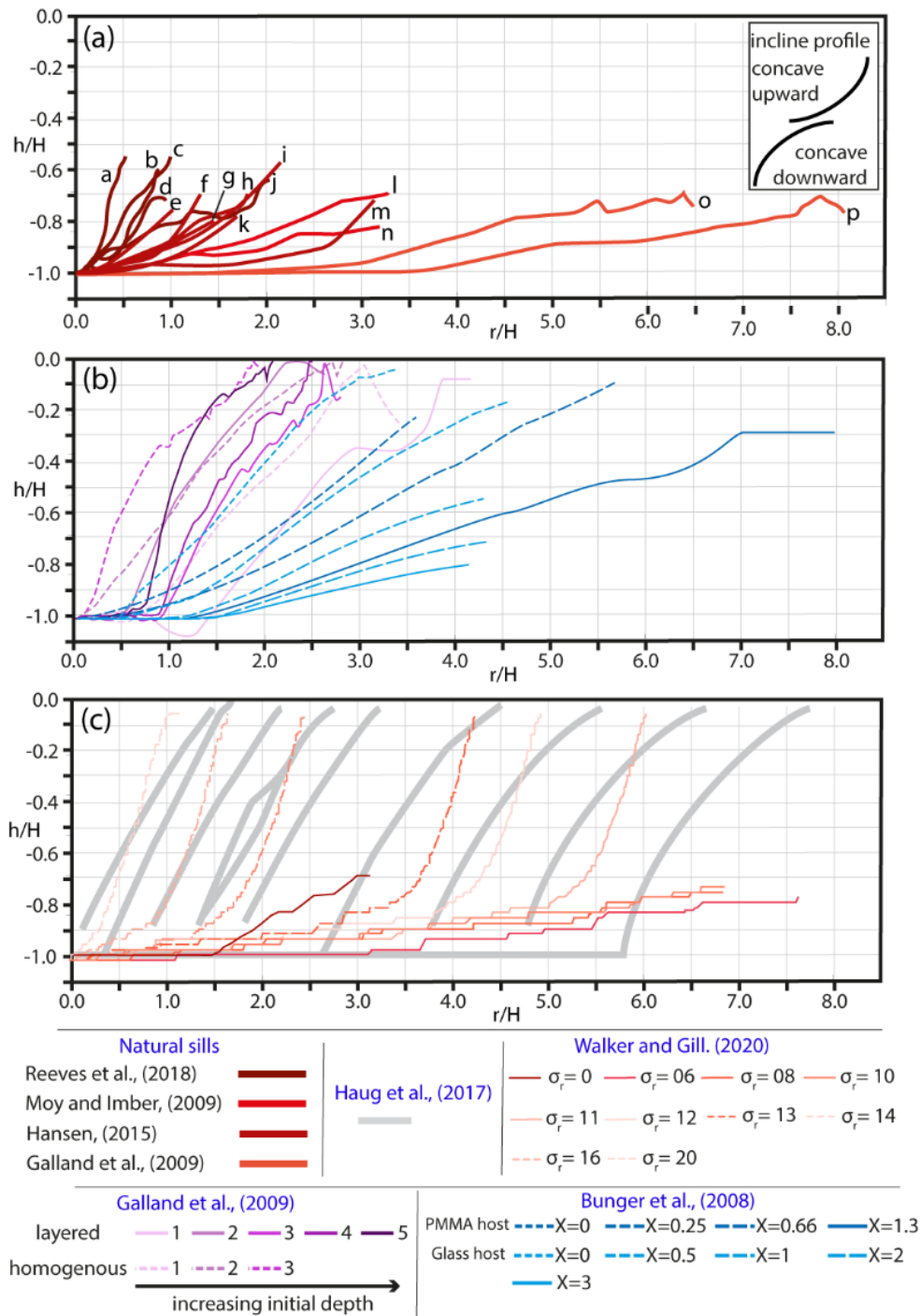
92 times their radius. This finding is supported by numerical (e.g. Malthe-Sørenssen. et al., 2004;  
 93 Walker and Gill, 2020) and analogue models (e.g. Bunger et al., 2008) using elastic host rocks,  
 94 which found that saucer-shaped sills form due to the mechanical interplay between elastic  
 95 deformation around the growing sill and upward displacement of the overburden towards a free  
 96 upper surface (Figs. 1b, d). However, models of Walker and Gill (2020) and Bunger et al.  
 97 (2008) require quite high horizontal stresses to produce geometries that approach those  
 98 observed in nature (Fig. 2c).



107 **Figure 1.** (a) Oblique aerial view of the Golden Valley sill in the Karoo basin, South Africa showing  
 108 an inner flat sill and outer inclined sheets (from Polteau et al. 2008). (b) Numerical simulation by  
 109 Malthe-Sørenssen et al. (2004) showing upward deflection due to the elastic interaction with the  
 110 overburden. (c) Schematic showing the overburden uplift and corresponding shear fault  
 111 development due to sill inflation, resulting in inclined sheets (from Galland et al. 2009). (d)  
 112 Numerical simulation by Gill and Walker (2020) showing the morphology of a saucer-shaped sill in  
 113 the absence of a horizontal tectonic compressional stress.

112 A recent numerical analysis by Haug et al. (2017) using rigid-plasticity theory in a  
 113 homogenous Mohr-Coulomb material showed that saucer-shaped sills can also be created due  
 114 to inelastic damage (i.e., shear failure) caused by an inflating flat sill (Fig. 2c). Furthermore,  
 115 analogue experiments using granular Mohr-Coulomb host-rock materials that undergo plastic  
 116 deformation also formed saucer-shaped sills (Mathieu et al., 2008; Galland et al., 2009) (Fig.

117 1c). However, inner sill to inclined sheet transitions, sill inclinations and overall geometries of  
 118 saucer-shaped sills of these numerical (Fig. 1b) and experimental models (Fig. 1c) do not match  
 119 with those in nature (Fig. 1a). Furthermore, experiments using brittle-elastic gelatine, a  
 120 common host rock analogue, have successfully produced sills and dykes but not saucer-shaped  
 121 sills (Kavanagh et al., 2006, 2015, 2018).



141 **Figure 2.** A comparison of saucer-shaped sill geometry in (a) nature, (b) experimental and (c)  
142 numerical models (modified after Walker and Gill, 2020). The axes plot sill radius ( $r$ ) against intrusion  
143 depth ( $h$ ), normalised by the overburden depth ( $H$ ). Experiments by Galland et al. (2009) (purple curves  
144 in Fig. 2b) used elasto-plastic silica powder as the host-rock analogue, while Bunger et al. (2008) used  
145 brittle-elastic glass or polymethyl methacrylate (PMMA) (blue curves in Fig. 9b). Numerical models  
146 by Walker and Gill (2020) (red curves in Fig. 2c) investigated how a horizontal compressive tectonic  
147 stress ( $\sigma_r$ ) in an elastic host influences saucer-shaped sill geometries. Haug et al. (2017) used a rigid-  
148 plasticity approach to simulate sills in homogenous Mohr-Coulomb material – grey curves in Fig. 2c  
149 plot damage zones, where magma is expected to intrude the host rocks, formed by inflation of horizontal  
150 cracks of variable starting length. Labels of saucer-shaped sills in nature represent; (a) Sill 2, (b) Sill  
151 1, (c) Sill 3 and (d) Sill 4 in Canterbury Basin, offshore SE New Zealand (Reeves et al., 2018); (e)  
152 Morskranes Sill, (f) Sundini Sill, (g) Kvívík Sill, (h) Fugloy Sill, (i) Eysturoy Sill, (k) Streymoy Sill and  
153 (m) Svínøy-Fugloy Sill in Faroe Islands (Hansen, 2015); (l) Eocene Sill 1 and (n) Eocene Sill 2 in  
154 Faroe-Shetland Basin (Moy and Imber, 2009); (o) Golden Valley Sill, South Africa and (p) Tulipan,  
155 Møre basin (Galland et al., 2009).

156 All of these saucer-shaped sill emplacement models assume ideally elastic or plastic  
157 end member rheological behaviour of host rocks. However, Earth's crust is thought to behave  
158 as a complex visco-elastic-plastic material (Ranalli, 2001; Bertelsen et al., 2018). Therefore,  
159 the models summarised above are likely not able to fully simulate the natural diversity of  
160 intrusion geometries, including the formation of saucer-shaped sills. Moreover, some models  
161 require quite high horizontal stresses to get those in nature (Fig. 2) (Bunger et al., 2008; Gill  
162 and Walker, 2020; Walker and Gill, 2020).

163 Most saucer-shaped sills in nature form in sedimentary basins that contain mechanically  
164 layered strata (Rivalta et al., 2005; Kavanagh et al., 2018). Sill intrusions modelled by  
165 Kavanagh et al., (2006, 2015) show that a layered system with a stiffer upper layer is required  
166 to create experimental sills. According to their experimental results, a weaker interface and the

167 higher rigidity contrast (i.e., Young's modulus ratio) between the layers play major roles in the  
168 formation and propagation of sills. This has been further supported by analogue experiments  
169 of saucer-shaped intrusions using granular materials (Galland et al., 2009), which found that  
170 mechanical layering is required to create the inner sills of saucer-shaped intrusions. However,  
171 Galland et al. (2009) did not test the effects of rigidity contrasts on saucer-shaped intrusion  
172 formation and propagation. Therefore, the effect of layering and its mechanical properties such  
173 as the Young's modulus ratio on the emplacement of saucer-shaped intrusions remain poorly  
174 understood.

175         Although field and 3D seismic reflection data have yielded a wealth of information  
176 about the geometries of saucer-shaped sills, field observations are limited due to the lack of  
177 well-preserved outcrops. Furthermore, 3D reflection seismic observations are limited by their  
178 spatial resolution, making it challenging to characterize intrusion geometries and associated  
179 structures related to their propagation. The geometries and emplacement mechanisms of  
180 saucer-shaped sills are therefore still poorly constrained and many fundamental questions  
181 remain to be answered. Such as, is it possible to reproduce the geometry of natural saucer-  
182 shaped sills in the laboratory using host rock analogues with complex visco-elastic-plastic  
183 rheology? What emplacement mechanisms control the development of saucer-shaped sills  
184 within complex host rock analogues? How do rigidity contrasts between stratigraphic layers  
185 influence the propagation of intrusions? Are high horizontal stresses strictly required to form  
186 natural saucer-shaped geometries?

187         Answering these questions requires experiments that simulate injection of a viscous  
188 liquid into a visco-elastic-plastic host material, and the ability to analyse the geometry of the  
189 resulting intrusions and associated host rock deformation. In this paper, we document the  
190 results of laboratory experiments in which paraffin oil (the magma analogue) is injected into  
191 visco-elastic-plastic Laponite RD<sup>®</sup> gels, simulating the upper crust. Our objectives are to

192 simulate the emplacement of saucer-shaped sills and to better constrain the mechanisms  
193 governing their fundamental geometry, including the effects of mechanical layering. The  
194 complex segmentation patterns that are observed at the margins of our model sills are the  
195 subject of a companion paper (Arachchige et al., in review) and only briefly presented here.

## 196 **2. Experimental methods**

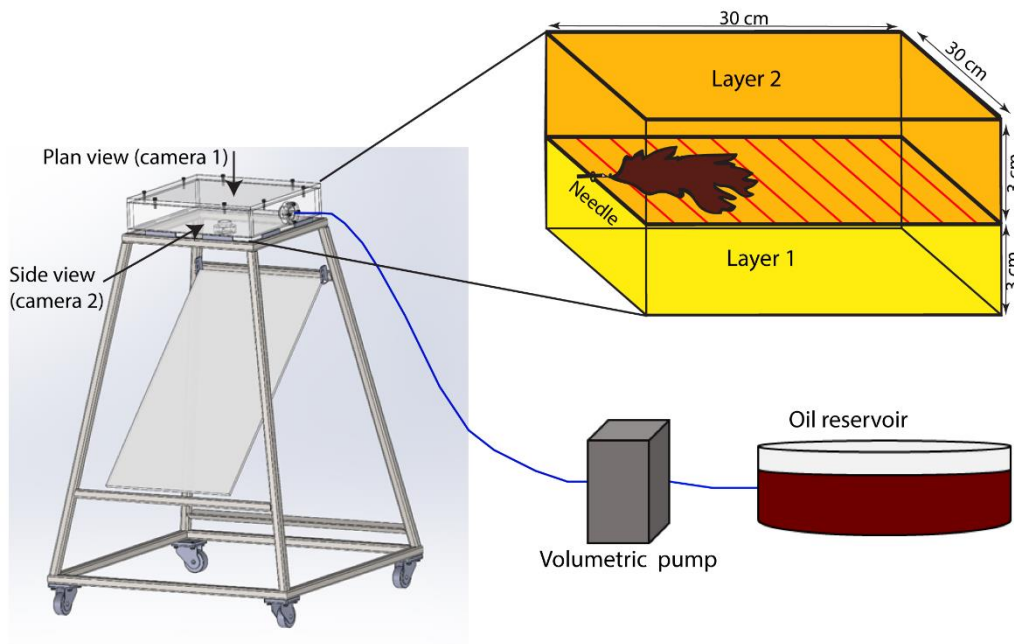
### 197 **2.1. Experimental setup**

198 Our experiments are designed to simulate the horizontal propagation of sills in the  
199 laboratory and to visualise the resulting lateral flow of analogue magma. The main objective  
200 of the experiments reported here is to investigate the emplacement and propagation of saucer-  
201 shaped intrusions in layered analogue host rocks. The experimental setup comprises a  
202 plexiglass tank (30 cm x 30 cm x 6 cm) filled with layers of Laponite RD® (LRD) gel as the  
203 upper crustal analogue (Layer 1 and Layer 2, Fig. 3). The upper surface of LRD in the tank is  
204 a free surface, while the vertical side walls and base of the tank are no-slip boundaries.  
205 Paraffin oil (magma analogue) is injected horizontally into the LRD using a tapered needle (2  
206 mm inner diameter) via a nozzle at the side of the tank fed by a peristaltic pump at a controlled  
207 volumetric flow rate. The experiments involve different volumetric flow rate of the intruding  
208 fluid, and the rigidity of the LRD layers. Fluid propagation is recorded by high resolution  
209 DSLR cameras (Fig. 3) placed above and at the side of the tank to capture the intrusion  
210 geometry and its evolution in plan and cross-sectional view, respectively.

### 211 **2.2. Image processing**

212 We use blue-channel pixel intensity values to map contour lines of the intrusion margin  
213 over time. Pixel intensity values at each time step ( $I$ ) are normalised by pixel intensity values  
214 at time step 0 (before the intrusion starts) ( $I_0$ ), resulting in  $I/I_0 = 1$  for the LRD host and  $I/I_0 <$   
215  $1$  for the intruding fluid. The  $I/I_0$  ratio is used to define a threshold for the intruding fluid, which  
216 is used to determine growth contour lines using a built-in ‘contour’ function in MATLAB.

217 Since growth contours have irregular shapes, we calculate best-fit circles to the contour line at  
 218 each time step and use the resulting radius to quantify horizontal sill growth rates. However,  
 219 the intrusion radius measurements are not corrected for the slope of the outer sill. Since the  
 220 images are captured in map view, growth contours for inclined outer sheet intrusions therefore  
 221 appear closer.  
 222



232 **Figure 3.** Schematic diagram of the experimental setup used in this study. A volumetric peristaltic pump  
 233 injects paraffin oil horizontally via a needle into either homogenous or two-layer Laponite RD<sup>®</sup> gel.  
 234 Two DSLR cameras capture the geometric details of sill propagation from top and side views.

235 **2.3. Analogue materials**

236 **2.3.1. Crustal host rock analogue**

237 The host rock analogue used in the experiments is Laponite RD<sup>®</sup> (LRD), a gel-forming  
 238 grade of synthetic smectite clay manufactured by BYK Additives and Instruments (2014).  
 239 Depending on its concentration, curing time and pH, LRD displays a wide range of viscoelastic  
 240 properties, with purely elastic and viscous domains (Bonn et al., 2002; Ruzicka and Zaccarelli,  
 241 2011; Kaushal and Joshi, 2014; Arachchige et al., 2021). When mixed with water, LRD forms

242 a transparent gel, which is similar to gelatine but is colourless and more transparent. Like  
243 gelatine, its photo-elastic properties can be used to visualize and map stresses associated with  
244 propagating fractures. LRD is a chemically and biologically stable material and it is easy to  
245 alter its mechanical properties, such as the Young's modulus, by changing its concentration.  
246 LRD has lower surface energy values (24 - 44 mJ/m<sup>2</sup>; Norris et al., 1993) compared to gelatine,  
247 a frequently used intrusion host rock analogue (1 J/m<sup>2</sup>; Kavanagh et al., 2013). This ensures  
248 that surface tension dynamics are minimized in geological analogue experiments using LRD.  
249 Rheological measurements of LRD reported by Arachchige et al. (2021) indicate that it is  
250 suitable for modelling the visco-elastic-plastic deformation of rocks, including elastic and  
251 plastic end members. Linear visco-elastic (LVE) behaviour occurs for shear strains,  $\gamma < 10\%$   
252 and strain rates of up to  $0.01 \text{ s}^{-1}$  for concentrations from 2 wt. % to 4 wt. % and a curing time  
253 of 72 hours. LRD starts to yield at shear strain  $\gamma = 10\%$  for concentrations 2 wt. % to 4 wt. %  
254 with yield strength of 25 to 200 Pa, respectively. Higher shear strains ( $\gamma > 26.2\%$ ) and strain  
255 rate  $\dot{\gamma} \geq 0.01 \text{ s}^{-1}$  must be maintained to model plastic deformation. The Young's modulus of 2  
256 wt. % to 4 wt. % LRD, with a curing time of 72 hours vary from  $1.05 \times 10^3$  to  $1.18 \times 10^4$  Pa,  
257 respectively. Here we use Young's modulus values of LRD as the main host rock variable and  
258 following Arachchige et al. (2021) assume that LRD is incompressible with Poisson's ratio =  
259 0.5.

### 260 **2.3.2. Magma analogue material**

261 We use paraffin oil at 22.5 °C as the magma analogue due to its non-reactive stability  
262 with LRD. Paraffin oil has a viscosity of 0.16 Pa s and the density of 850 kg m<sup>-3</sup> at this  
263 temperature. The magma analogue was mixed with red dye without altering its viscosity to  
264 provide a better visual contrast with the host material.

265 **2.4. Scaling**

266 Our experiments are approximately scaled to nature (Table 1) using methods developed  
 267 by Hubbert (1937), Ramberg (1982), Merle and Borgia (1996), Mathieu et al. (2008), Galland  
 268 et al. (2009) and Arachchige et al. (2021). The principle is to define scaling factors and  
 269 dimensionless numbers for the model, which ensure approximate geometric, kinematic and  
 270 dynamic similarity to processes in nature.

271 **Table 1.** Symbols, units and values of variables in nature and model for scaling factors and  
 dimensionless ratios. See equation 5 and 6 for  $\Pi_4$  and  $\Pi_5$ .

Parameter	Units	Definition	Value		
			Nature (p)	Model (m)	Ratio*(m/p)
$\rho_c$	kg m <sup>-3</sup>	Density of host rock	2800	1000	0.357
$\rho_m$	kg m <sup>-3</sup>	Density of magma	2700	850	0.3
G	m s <sup>-2</sup>	Gravity acceleration	9.81	9.81	1
$V_i$	m s <sup>-1</sup>	Velocity of intrusion	0.2	10 <sup>-5</sup>	5 · 10 <sup>-5</sup>
L	m	Length	100	0.01	10 <sup>-4</sup>
t	s	Time	-	900-2700	2 · 10 <sup>-2</sup>
$\mu$	Pa s	Viscosity of intrusion	2.2 x 10 <sup>5</sup>	0.16	7.14 x 10 <sup>-7</sup>
$Q_i$	m <sup>3</sup> s <sup>-1</sup>	Volumetric flow rate of intrusion	(0.02 - 13.28)	- 8.3 x 10 <sup>-9</sup>	(6.25 x 10 <sup>-10</sup> - 3.75 x 10 <sup>-7</sup> )
Definition of dimensionless ratios			Nature	Experiment	
$\Pi_1$	Intrusion thickness (T)/length (L)		~ 10 <sup>-2</sup>	~ 10 <sup>-2</sup>	
$\Pi_2$	Intrusion thickness (T)/depth (H)		0.06 – 0.66	0.03 – 0.10	
$\Pi_3$	Intrusion height (h)/length (L)		0.2 – 0.3	0.3	
$\Pi_4$	Inertial/viscous forces		2.5 x 10 <sup>-6</sup> – 270	(5.6 – 12.4) x 10 <sup>-4</sup>	
$\Pi_5$	Magma/country rock densities		-0.08 – 0	0.14	
Stress scaling factor		$\sigma^* = \rho^*g^*L^* = 3.57 \times 10^{-5}$ Model is 10 <sup>5</sup> times weaker than in nature			
Time scaling factor		$t^* = L^*/V^* = 2 \times 10^{-2}$ 1 min in model ~ 0.83 hr in nature			
Viscosity scaling factor		$\mu^* = t^*\sigma^* = 7.14 \times 10^{-7}$ Model intrusion represents a magma viscosity of 10 <sup>4</sup> Pas			
Volumetric flow rate scaling factor		$Q^* = \Delta\rho^*L^{*3}E^{*-1}V^* = 6.25 \times 10^{-10} - 3.75 \times 10^{-7} \text{ m}^3\text{s}^{-1}$ Model volumetric flow rates = 0.02 – 13.28 m <sup>3</sup> s <sup>-1</sup> in nature			

272

273 We define the length scale factor ( $L^*$ ) as the ratio between the overburden depth of the  
 274 sill in the model (subscript m) to one in the shallow crust (subscript p), which is initially taken

275 as  $10^{-4}$  (1 cm represents 100 m). The ratio between the density of LRD in our experiments and  
276 that of the natural host rocks ( $\rho^*$ ) is  $\sim 0.36$  and the gravitational acceleration is the same in our  
277 experiments and in nature ( $g^* = 1$ ). Thus, the stress scaling factor is:

$$278 \quad \sigma^* = \rho^* g^* L^* = 3.6 \times 10^{-5} \quad (1)$$

279 Comparing the average model intrusion tip velocity of  $\sim 1 \times 10^{-3} \text{ ms}^{-1}$  to an estimated  
280 natural magmatic intrusion velocity of  $0.2 \text{ ms}^{-1}$  (range between  $0.1 \text{ ms}^{-1}$  and  $0.5 \text{ ms}^{-1}$ ; Spence  
281 and Turcotte, 1985; Kavanagh et al., 2013) gives a velocity scaling factor,  $V^* = 5 \times 10^{-3}$ . We  
282 can now define the time scaling factor as

$$283 \quad t^* = L^*/V^* = 2 \times 10^{-2} \quad (2)$$

284 Therefore, 1 min in our experiments represents 50 min in nature. Using  $\sigma^*$  and  $t^*$ , the viscosity  
285 scaling factor becomes

$$286 \quad \eta^* = \sigma^* t^* = 7.2 \times 10^{-7} \quad (3)$$

287 So paraffin oil (magma analogue) with a viscosity of  $0.16 \text{ Pas}$  is equivalent to a magma in  
288 nature with a viscosity of  $10^4 \text{ Pas}$ , consistent with basaltic andesite with low crystal content  
289 (Persikov, 1991; Mathieu et al., 2008).

290 The measured Young's modulus,  $E$ , of LRD concentrations after 7 days curing time  
291 used in the experiments is  $10^3 - 10^4 \text{ Pa}$  (see Arachchige et al., 2021). Since  $E$  of upper crustal  
292 sedimentary rocks is typically in the range of  $10^9 - 10^{10} \text{ Pa}$  (Kavanagh et al., 2013), the Young's  
293 modulus scaling factor,  $E^*$  in our experiments is  $10^{-7} - 10^{-5}$ . Therefore, based on  $\sigma^*$  and  $E^*$  our  
294 model host rock is  $\sim 10^5$  times weaker than in nature.

295 With the exception of one experiment (10A), the volumetric flow rate of intruding  
296 magma in our experiments is kept constant, and only the Young's modulus of the host rock  
297 layers is varied between experiments. The only input geometric variable is the Layer 2  
298 overburden depth,  $H$  (Fig. 2). Output geometric variables are the intrusion length,  $L$ , thickness,

299 T, and the vertical height of the intrusion (i.e., intrusion depth), h, relative to the interface  
300 between the horizontal layers or the injection needle.

301 Following the Buckingham- $\Pi$  theorem (Barenblatt, 2003; Galland et al., 2009), we  
302 define five independent dimensionless numbers that characterise the system (Table 1), which  
303 are used to assess the geometrical, kinematic and dynamic similarities between the experiments  
304 and nature. The first three dimensionless numbers are the geometric ratios of the system:

305

$$306 \quad \Pi_1 = T/L,$$

$$307 \quad \Pi_2 = T/H, \tag{4}$$

$$308 \quad \Pi_3 = h/L.$$

309 The length, L, and the thickness, T, of shallow crustal sills in nature are typically in the  
310 range of 10 – 100's km and 20 – 200 m respectively (Galland et al., 2009; Cruden et al, 2017).  
311 Therefore,  $\Pi_1$  in nature is in the order of  $10^{-2}$ . Experimental sill lengths and thicknesses vary  
312 between 5 – 9 cm and 1 – 3 mm, respectively, so  $\Pi_1$  is also on the order of  $10^{-2}$ . Overburden  
313 depth, D, is 3 cm in the experiments and 100 – 3000 m in nature. Thus,  $\Pi_2$  ranges between 0.03  
314 – 0.1 and 0.006 – 2 in the experiments and nature, respectively. Calculated  $\Pi_3$  values range  
315 from 0.22 to 0.56 for the experiments, and are estimated to be around 0.3 in nature (Mathieu et  
316 al., 2008). The geometric dimensionless numbers of the models are therefore close to the  
317 natural values, indicating approximate geometric similarity.

318 The Reynolds number, which is the ratio of inertial to viscous forces in a flow,  
319 establishes if the flow regime within the intrusion is laminar or turbulent:

$$320 \quad \Pi_4 = Re = \frac{\rho_m TV}{\eta} \tag{5}$$

321 where  $\rho_m$  is the density and  $\eta$  is the viscosity of magma. In the experiments,  $\Pi_4$  varies between  
322  $8 \times 10^{-3}$  to  $1.6 \times 10^{-2}$ . Therefore, viscous forces are dominant, inertial forces are negligible and  
323 the flow is laminar (i.e.,  $Re \ll 2300$ ). Reynolds numbers for magma flow within dykes and

324 sills in nature varies from  $2.5 \times 10^{-6}$  to 270 for felsic and mafic magma respectively (Galland  
325 et al., 2009). Therefore, the Reynolds numbers in our experiments are consistent with those in  
326 nature, where magma flow is usually laminar.

327 The final dimensionless number is the ratio of the magma and the host rock density,  
328 corresponding to the buoyancy of the magma, which can be expressed by:

$$329 \quad \Pi_5 = 1 - \frac{\rho_m}{\rho_c} \quad (6)$$

330 Where  $\rho_c$  the density of the upper crustal host rocks. In our experiments,  $\Pi_5 = 0.15$  and in nature  
331 it varies between -0.8 to 0 in the shallow crust (Galland et al., 2009), indicating that magma is  
332 neutrally to negatively buoyant. In the experiments the analogue magma is slightly positively  
333 buoyant. However, as most sills form and propagate as horizontal to sub-horizontal cracks,  
334 buoyancy effects are negligible (Lister and Kerr, 1991; Kavanagh et al., 2006; Galland et al.,  
335 2009) in both nature and experiments.

### 336 **3. Experimental results**

337 Here we present the outcomes of experiments with two different initial setups. In the  
338 first setup, the upper crust is represented by a single homogeneous layer. In the second setup,  
339 the crust comprises two layers with different LRD concentrations and therefore different  
340 Young's moduli (Table 2). In both setups the viscosity of the intruding fluid and the intrusion  
341 depth were kept constant, as was the volumetric injection rate, with the exception of Exp. 10A.

#### 342 **3.1. Single layer experiments**

343 When paraffin oil was injected into homogenous LRD with concentration of 3 wt. %  
344 (Exp. 7, Table 2), the intrusion formed a horizontal crack (i.e., a sill) that propagated away  
345 from the injection point and then at  $\sim 360$  s deviated upwards toward the free surface as a steeply  
346 inclined sheet (Fig. 4a). The propagating front of the intrusion developed irregular finger-like  
347 protrusions at the onset of steep upward propagation. At this stage, a narrow high-flow channel

348 also started to form from the injection point, which migrated through the flat sill into the  
 349 inclined sheet (Fig. 4a).

350 **Table 2.** Summary of experiments and parameters

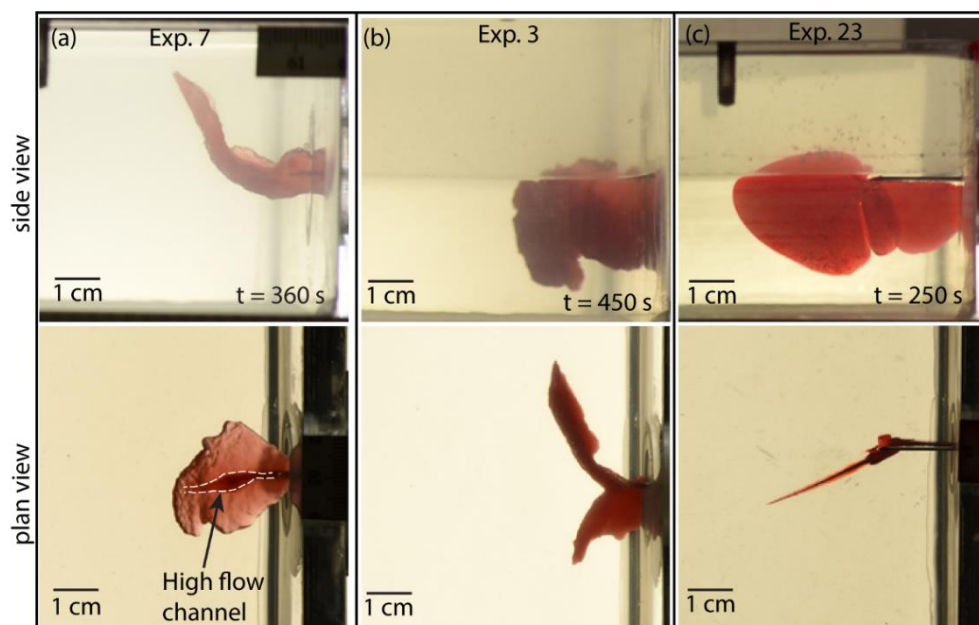
No	$X_{LL}$	$\rho_{LL}$	$E_{LL}$	$X_{UL}$	$\rho_{UL}$	$E_{UL}$	$E_{UL}/E_{LL}$	$\theta$	comments
7	3	1050	5013	-	-	-	-	71	Planar crack
3	2.5	1045	2405	4	1075	10266	4.27	-	Vertical crack in bottom layer
5	3	1050	5013	4	1075	10266	2.05	18.5	Flat sill to inclined saucer
6	3	1050	5013	3	1050	5013	1	17.8	Flat sill to inclined saucer
9	3.5	1060	8317	4	1075	10266	1.23	21.7	Flat sill to inclined saucer
10	4	1075	10266	4	1075	10266	1	16.3	Flat sill to inclined saucer
19	3.5	1060	8317	4	1075	10266	1.23	24.5	Flat sill to inclined saucer
23	2	1040	1216	4	1075	10266	8.44	-	Vertical crack in bottom layer
30	3.5	1075	8317	3.5	1060	8317	1	17.1	Flat sill to inclined saucer
10A <sup>§</sup>	4	1075	10266	4	1075	10266	1	19.5	Flat sill to inclined saucer

351  $X$  = concentration of Laponite RD<sup>®</sup> (LRD) in deionised water (wt. %);  $\rho$  is density of LRD ( $\text{kg m}^{-3}$ );  $E$   
 352 = Young's modulus of LRD (Pa);  $\theta$  = inclination.  $E_{UL}/E_{LL}$  = rigidity ratio

353  
 354 Subscripts LL = lower layer and UL = Upper Layer.

355 <sup>§</sup>The injection volumetric flow rate in all experiments,  $Q = 1 \text{ ml/min}$ , except experiment 10A where  $Q$   
 356 =  $5 \text{ ml/min}$

357



367 **Figure 4.** (a) Intrusion propagation styles in a homogenous Laponite RD<sup>®</sup> gels with concentrations 3  
368 wt. % (Exp. 7). (b) Plan and side views of layered experiments with high rigidity ratio ( $E_r > 4$ ); Exp. 3  
369 (left panel) and Exp. 23 (right panel). Vertical cracks (dykes) formed within the lower concentration  
370 (Layer 1). See Table 2 for experimental details.

### 371 **3.2. Two-layer experiments**

372 In two-layer experiments, the magnitudes of the Young's moduli of the LRD layers (L1  
373 and L2), and the rigidity ratio,  $E_r = E_{UL}/E_{LL}$  were varied systematically, while the viscosity of  
374 the intruding fluid and the volumetric flow rate were kept constant, with the exception of Exp.  
375 10A (Table 2). The non-dimensional Young's modulus ratio,  $E_r$ , was found to be useful for  
376 explaining the first-order morphology of the model intrusions. However, second order features  
377 of the intrusions, such as marginal lobes and fingers are controlled by additional parameters,  
378 which are discussed in more detail in Arachchige et al. (in review). In most two-layer  
379 experiments, an initially planar, sub-horizontal crack formed along the L1/L2 interface and, at  
380 a certain point, turned upwards to form an inclined sheet, making a saucer-shaped sill that  
381 eventually erupted at the upper free-surface. The behaviour for high and low rigidity ratios is  
382 markedly different and we will explore the details in the following two subsections.

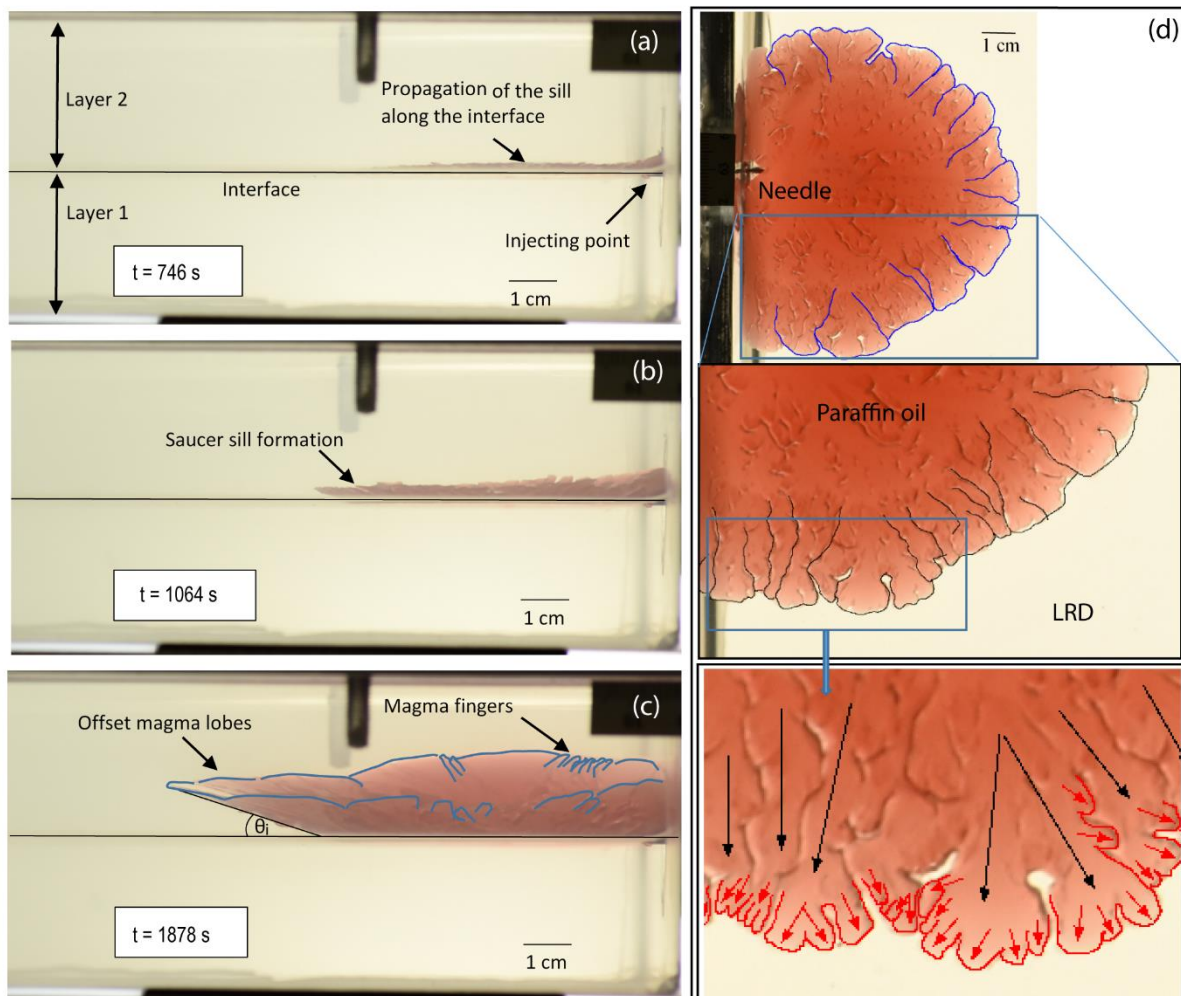
#### 383 **3.2.1. Case 1: Two-layer experiments with high rigidity ratio ( $E_r > 4$ )**

384 In two-layer experiments with a high rigidity ratio,  $E_r > 4$  (Fig. 4b), the injected paraffin  
385 oil formed vertical cracks that propagated downwards from the injection point. These dyke-  
386 like intrusions were limited to the much weaker, lower layer, which had LRD concentrations  
387  $X_L = 2.5$  and 2 wt. % in Exp. 3 and 23, respectively (Fig. 4b; Table 2). The propagating fronts  
388 of these intrusions were smooth, without segmentation or finger-like protrusions.

#### 389 **3.2.2. Case 2: Two-layer experiments with low rigidity ratio ( $E_r < 4$ )**

390 In all two-layer experiments with a lower rigidity ratio,  $E_r < 4$ , model intrusions initially  
391 propagated along the L1/L2 interface as inner flat, penny-shaped sills (Fig. 5a). These sills  
392 subsequently bent upwards together with overburden uplift as they intruded the upper layer,

393 forming inclined sheets (Fig. 5b and supplementary movie 1). The inclination,  $\theta_i$  of these  
 394 inclined sheets relative to the L1/L2 interface was  $15^\circ - 25^\circ$ , becoming steeper as they  
 395 approached the free surface (Fig. 5c). The propagating fronts of both the inner flat sill and the  
 396 outer inclined sheets consisted of lobes and finger-like segments that appeared at early stages  
 397 of growth. When primary individual lobes reach a critical width, they bifurcate into secondary  
 398 smaller lobes and finger-like segments (Fig. 5d). During the propagation of the inner flat sill  
 399 these lobes and fingers were confined to the 2D plane of the L1/L2 interface. However, once  
 400 the inclined sheets entered the upper layer, these segments developed 3D morphologies,  
 401 forming vertically offset, en-échelon structures (Fig. 5c)



402 **Figure 5.** Side views (left panels) and top views (right panels) of sill propagation in a two-layer  
 403 experiment (Exp. 6) as a function of time ( $T$ ). (a) Propagation of the inner sill along the two layer  
 404 interface. (b) Onset of outer, inclined sill formation. (c) Offset lobes and fingers forming at the

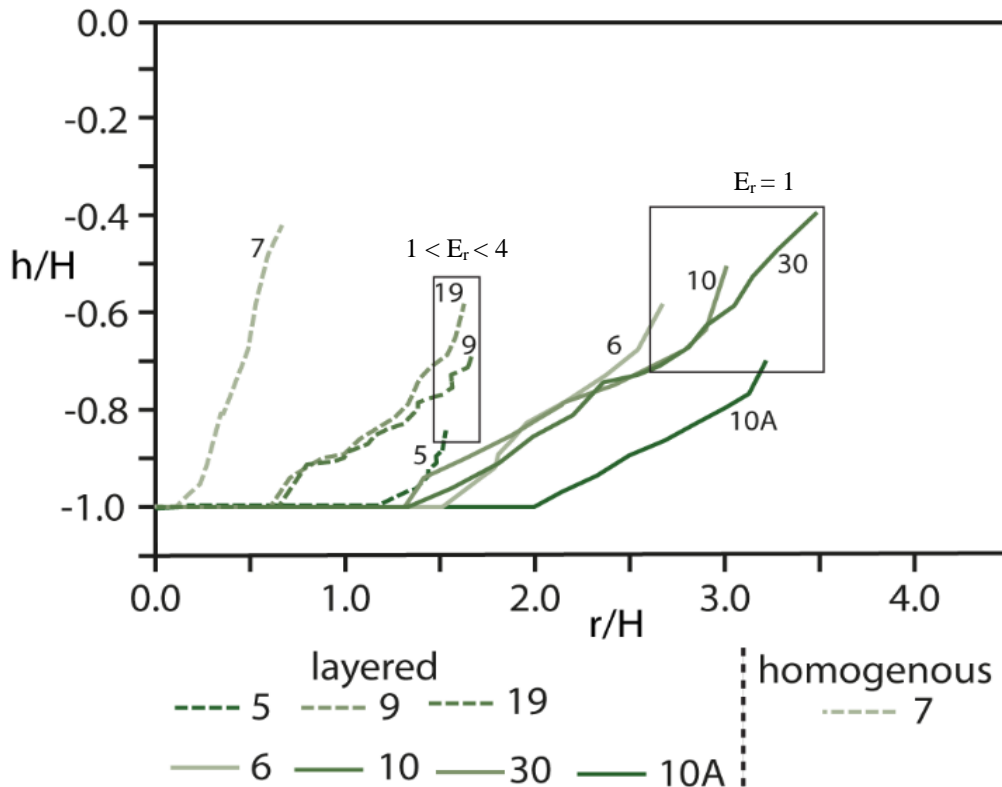
405 *propagating sill margin.  $\theta_i$  is the dip of the inclined sheet. (d) Formation and propagation of lobes and*  
406 *magma fingers and associated magma pathways. Paraffin oil (red) is injected from the left through a*  
407 *needle into transparent Laponite RD<sup>®</sup>. The sill expands radially and breaks into lobes and fingers. Lobe*  
408 *segments show distinct primary (blue) and secondary margins (black) and final magma transport*  
409 *directions (black and red arrows).*

410         Figure 6 plots the vertical profiles of all saucer-shaped sills formed in the one- and two-  
411 layer experiments, in which the intrusion height ( $h$ ) and the radius ( $r$ ) are normalised by  
412 overburden depth ( $H$ ). The transition radius from the inner sill to the outer inclined sheet occurs  
413 over a range of  $r/H$  values and the inclined sheets have variable inclinations,  $\theta_i$ . The single layer  
414 experiment (Exp. 7) has the smallest transition radius ( $r/H < 0.5$ ) and the steepest outer sheet  
415 inclination ( $71^\circ$ ). In two-layer experiments with  $1 < E_r < 4$  (Exp. 5, 9 and 19), the transition  
416 radius occurs at  $r/H = 0.5 - 1.25$ , with much shallower outer sheet inclination angles ( $15^\circ$ - $25^\circ$ ).  
417 However, these inclination angles vary by  $2^\circ - 3^\circ$  in Experiments 5, 9 and 19, indicating a  
418 small degree of uncertainty. Experiments 9 and 19 differ from experiment 5 in that  $E_{LL}$  is  $\sim 81\%$   
419 of  $E_{UL}$ , whereas in Experiment 5 this is  $\sim 49\%$ . Therefore, sill inclinations are substantially  
420 different between experiments, reflecting the relative difference in stiffness between layers. In  
421 experiments with  $E_r = 1$  (Exp. 6, 10, 10A, 30), the inner flat sills are considerably wider and  
422 the transition to the outer inclined sheet occurs at  $r/H = 1 - 1.5$  with similar  $\theta_i$  angles to the  $1 <$   
423  $E_r < 4$  experiments. However, as the relative stiffness increases between Experiment 6 to 30,  
424 the inner sill appears to increase in length and the inclination angles are similar. By comparison,  
425 the only difference between Experiments 6 and 7 is the interface between the layers in  
426 Experiment 6, but it has a much longer inner flat sill with same inclination angle (Fig. 6).

### 427 **3.3. Growth and propagation of the inner and outer sills**

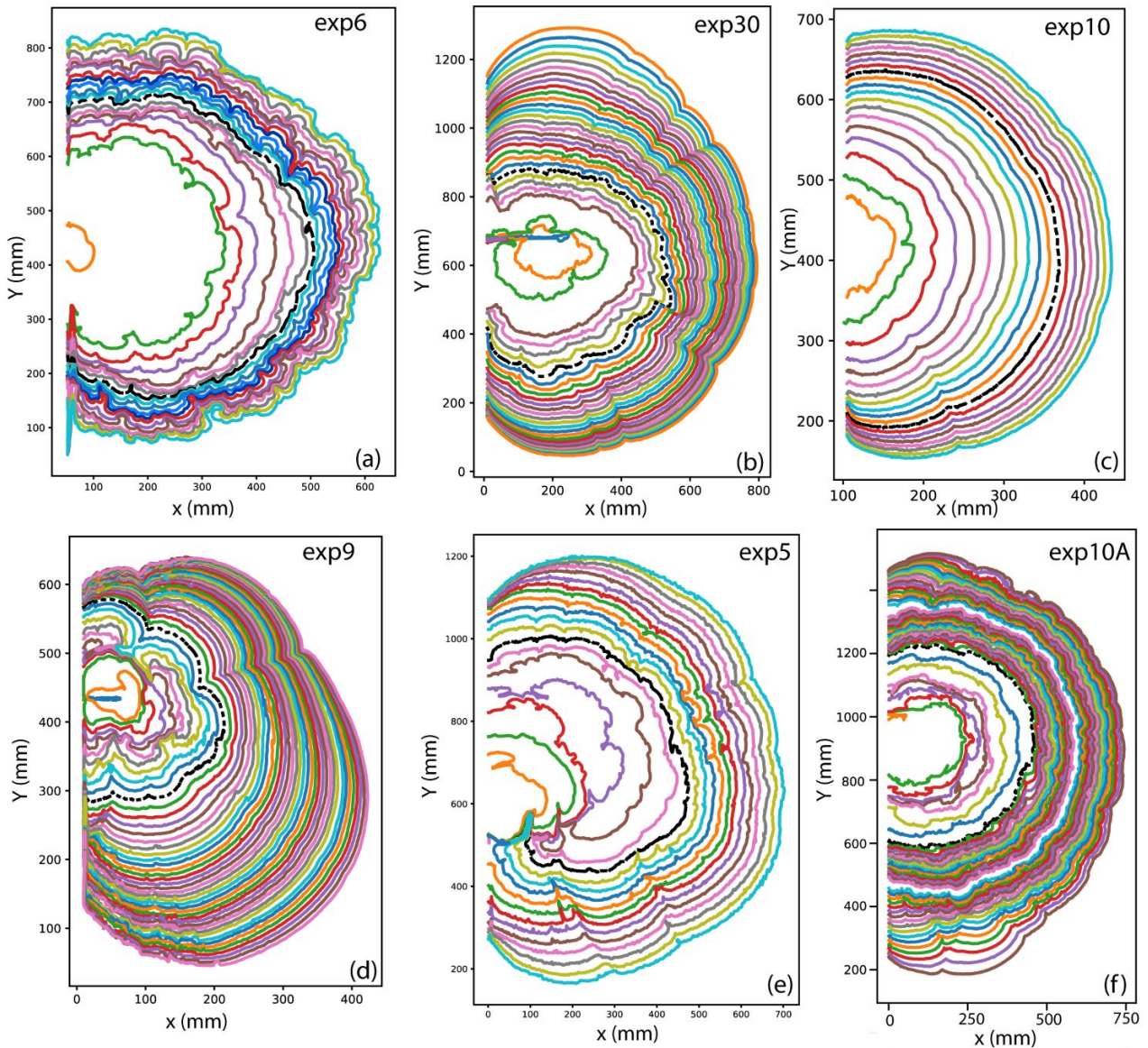
428         Growth contour maps of the propagating fronts of saucer-shaped sills with rigidity  
429 ratios  $E_r < 4$  are shown in Figure 7. Because the maps are in plan view, growth contours within  
430 the inclined sheets appear more closely spaced than the inner flat section of the sill. Propagation

431 styles for experiments with  $E_r = 1$  (Exp. 6, 30, 10) vary systematically as the absolute value of  
 432  $E$  and concentration of LRD increases within Layer 2. For  $E_r = 1$  and an LRD concentration of  
 433 3 wt. % in L1 and L2 (Exp 6; Fig. 5d and 7a, Table 2), the intrusion propagated with a highly  
 434 segmented margin characterised by finger-like and lobe structures. The absence of contours at  
 435 early time steps is due to the unavailability of images due to a momentary camera failure. In  
 436 Exp. 30 (Fig. 7b), with L<sub>1</sub> and L<sub>2</sub> concentration = 3.5 wt. %, growth contours indicate a  
 437 propagation front with moderately developed segments. When the L<sub>1</sub> and L<sub>2</sub> LRD  
 438 concentration = 4 wt. % in Exp. 10, the growth contours are smooth, indicating a planar  
 439 propagation front with very weak to no segmentation (Fig. 7c). Two-layered experiments with  
 440  $E_r > 1$  also have moderately segmented propagating fronts (Figs. 7d-f, similar to those in Exp.  
 441 30 (Fig.7b).



452 **Figure 6.** Normalised vertical profiles of sills observed in homogeneous and two-layer experiments.  
 453 The shortest inner sill and the steepest outer sill are formed by the homogenous layer experiment (Exp.  
 454 7). In layered experiments, the outer sill profiles are concave upward, becoming steeper toward the  
 455 upper surface.

456 The intrusion radius measured in plan view from best fit circles to the growth contours  
 457 at each time step are plotted against time in Figure 8 for all two-layer experiments with  $E_r < 4$ .  
 458 The inner-outer sill transition radius is marked for each experiment (i.e. black dotted line). The  
 459 horizontal growth rates (i.e. slopes) of the intrusions with  $Q_i = 1$  ml/min vary between 0.45 and  
 460 0.55 mm/s.



461 **Figure 7.** Contour maps of sill margins over time calculated with image analysis. The contour interval  
 462 is 25 s for all panels except exp.10A (10 s) and the dotted black contours on each map represent the  
 463 contour at the inner to outer sill transition. The empty space in (a) (Exp. 6) is due to missing images  
 464 due to camera failure at the early stages of the experiment.

### 3.4. Influence of volumetric flow rate, $Q_i$

To determine the effect of a higher volumetric injection flow rate, we repeated Exp. 10 (Fig. 7c) in Exp. 10A with  $Q_i = 5$  ml/min rather than 1 ml/min. This resulted in the largest inner-outer sill transition radius  $r/H \sim 2$  observed in the two-layer experiments and a similar  $\theta_i$  angle (Fig. 6). As expected, the horizontal growth rate of Exp. 10A is higher than the experiments with  $Q_i = 1$  ml/min, with a value of 0.61 mm/s compared to  $\sim 0.5$  mm/s.

In contrast to the planar sill margin developed in Exp. 10, growth contours for Exp. 10A (Fig. 7f) indicate a complex and strongly segmented propagation front, similar to Exp. 6 (Fig. 7a). This implies that the nature of the propagating front is controlled not only by the absolute value of  $E$  in Layers 1 and 2 (cf. Figs. 7a-c and f), but also on the volumetric injection flow rate of the analogue magma.

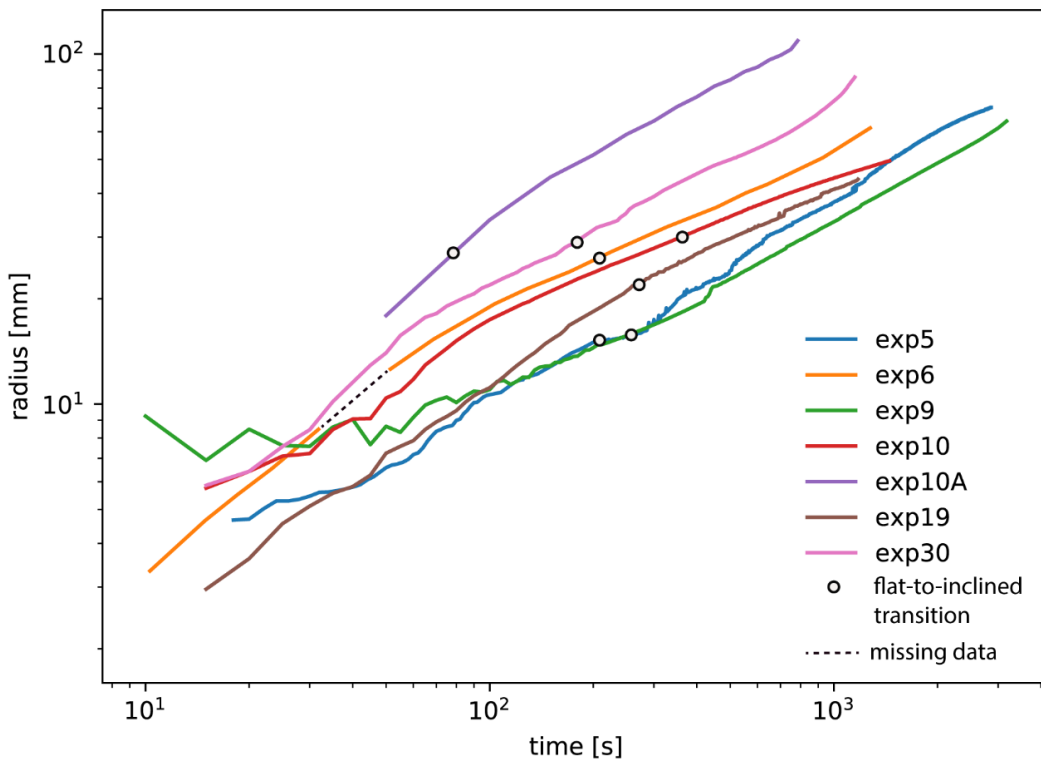


**Figure 8.** The average radius for sills in experiments (in map view) with rigidity ratio  $E_r < 4$  plotted as the best fit radius against time. The black open circles on each curve represent the transition from inner flat sill to inclined sheet of saucer-shaped intrusions. See Table 2 for the details of the experiments.

## 491 **4. Discussion**

### 492 **4.1. General considerations**

493           The first-order geometries (i.e. saucer-shape, sill inclination) of intrusions formed in  
494 our experiments match the major features of mafic sills observed in nature, particularly those  
495 in sedimentary basins. Our homogenous and two-layer experiments (except the vertical dyke  
496 in Exp. 4b) reproduced the three-dimensional shape of saucer-shaped sills with a horizontal  
497 inner sill, emplaced along a horizontal interface in two-layer experiments, followed by a sharp  
498 transition to an outer, inclined sheet. Furthermore, the margins of both inner sills and outer  
499 inclined sheets in the experiments developed non-planar intrusion fronts with lobes and finger-  
500 like structures that are similar to marginal features of saucer-shaped sills observed in 3D  
501 seismic reflection seismic data (Thomson and Hutton, 2004; Hansen and Cartwright, 2006) and  
502 the marginal lobes developed on propagating sills during solidification experiments  
503 (Chanceaux and Menand, 2016). Our 3D experimental results also support the results of 2D  
504 numerical simulations of saucer-shaped intrusions (Malthe-Sørensen et al., 2004; Walker and  
505 Gill, 2020). We therefore suggest that our model results provide insights into mechanical  
506 processes governing the emplacement of mafic sills in sedimentary basins.

### 507 **4.2. Emplacement of the inner sill**

508           In homogenous layer experiments, paraffin oil that was injected into low and moderate  
509 concentrations of LRD formed either a spherical blob (Arachchige et al., 2021) or a very short  
510 inner sill followed by a very steep outer sheet (Fig. 4a), respectively. In contrast, in two-layer  
511 experiments with low rigidity ratio ( $E_r < 4$ ), paraffin oil injection always resulted in the  
512 formation of flat inner sills with large diameters (Fig. 4), whereas in experiments with high  
513 rigidity ratio ( $E_r \geq 4$ ), a sub-vertical intrusion propagated in the weaker lower layer only (L1;  
514 Exp. 3 and 23, Fig. 4b). These results suggest that the formation of larger diameter, flat-lying  
515 sills requires the presence of layering in host rocks with low rigidity ratios ( $E_r < 4$ ). This

516 conclusion is supported by previous experiments with a layered setup (Kavanagh et al., 2006,  
517 2015; Galland et al., 2009) and numerical calculations (Barnett and Gudmundsson, 2014). In  
518 detail, the propagating margin of the inner sill in both homogenous and layered experiments is  
519 typically non-planar and often consists of finger-like and lobate segments (Fig. 5d). Such  
520 complex segmentation was not observed in previous laboratory experimental models of sills  
521 using gelatine or granular host media (Mathieu et al., 2008; Galland et al., 2009; Kavanagh et  
522 al., 2015). However they are often described from mafic sills in sedimentary basins (Magee et  
523 al., 2016; Spacapan et al., 2017) and 3D seismic reflection data (Hansen and Cartwright, 2006).  
524 A detailed discussion of these irregular short-wavelength (in relation to the total intrusion  
525 length scale) features and their formation is beyond the scope of the present paper and they are  
526 analysed in detail in Arachchige et al. (in review).

#### 527 **4.3. Inner sill to inclined sheet transition**

528 The transition from a flat inner sill to an inclined outer sheet, characteristic of all saucer-  
529 shaped sills, has been discussed in previous analytical, numerical and laboratory modelling  
530 studies (Pollard and Holzhausen, 1979; Polteau et al., 2008; Galland et al., 2009; Gill and  
531 Walker, 2020). These previously published models of saucer-shaped sills display either smooth  
532 (curved) or sharp inner to outer sill transitions when the magma or magma analogue intrudes  
533 homogenous or layered host rocks, respectively. Our experiments produce similar smooth (Figs.  
534 4a, 6) and sharp (Figs. 5, 6) transitions in homogenous and two-layer experiments, respectively.  
535 This suggests that layering exerts a primary control on the formation of sharp transitions to  
536 inclined sheets, but it is not a prerequisite to form saucer-shaped sills. Field observations of  
537 sills in layered host rocks also confirm the presence of sharp inner to outer sill transitions (e.g.  
538 Chevallier and Woodford, 1999; Polteau et al., 2008).

539 Several hypotheses have been proposed to explain the mechanics of the inner to outer  
540 sill transition. Inspired by the behaviour of near surface hydraulic fractures, linear elastic

541 fracture mechanics (LEFM) approaches interpret this transition in the framework of the  
542 interaction between horizontally growing cracks and Earth's free surface (Pollard and  
543 Holzhausen, 1979; Fialko et al., 2001; Malthe-sørenssen et al., 2004; Bungler and Detournay,  
544 2005; Bungler et al., 2005, 2008; Gill and Walker, 2020). Numerical experiments by Malthe-  
545 Sørenssen et al. (2004) show that when sills reach a radius approximately equal to the  
546 overburden depth (i.e.,  $r/H \sim 1$ ), their shapes start to become asymmetrical, which results in  
547 inflation induced bending of the overburden. Consequently, the stress in front of the sill tip  
548 becomes asymmetrical and the sill branches upwards. Fialko et al. (2001) theoretically  
549 predicted that the inclination,  $\theta_i$ , of the outer sill should vary from  $1^\circ$  to  $35^\circ$  as  $r/H$  changes  
550 from 0.5 to 5, respectively. These theoretical  $\theta_i$  values are within the range of those observed  
551 in natural saucer-shaped sills, where  $\theta_i = 10^\circ$  to  $30^\circ$  (Malthe-Sørenssen. et al., 2004; Galland  
552 et al., 2009).

553 In comparison, in assuming that the host rocks are Mohr-Coulomb materials, numerical  
554 analysis by Haug et al. (2017) suggests that the inner to outer sill transition occurs due to the  
555 formation of a localized plastic shear damage zone (or shear failure zone) at the tip of a growing  
556 sill. In this model, the inflating inner flat sill triggers the formation of shear failure zones that  
557 propagate from the sill tip to the Earth's surface, which then provides an inclined pathway for  
558 subsequent magma flow and outer sill formation. However, all of the saucer-shaped sill profiles  
559 of Haug et al. (2017) have inclination angles,  $\theta_i \geq 60^\circ$ , which is much steeper than those  
560 observed in nature. The magma overpressure required for shear failure of the overburden in  
561 Haug et al.'s (2017) model varies from 100's of MPa to 60MPa for sills with  $r < 2$  km and a  
562 few MPa for larger sills with  $r > 2$  km. However, magma overpressure estimates in nature are  
563 typically in the range of 1 – 20 MPa (Rubin, 1995). Therefore, Haug et al. (2017) argue that  
564 localized shear failure of the overburden is only favoured for larger sills ( $r > 2$  km) when  $r/H > 1$ .  
565 Localized shear failure of the overburden during saucer-shaped sill formation has also been

566 reproduced in laboratory experiments that used Mohr-Coulomb, elasto-plastic host rock  
567 analogues, in which the formation of inclined outer sheets was attributed to plastic deformation  
568 and the formation of shear zones (Galland et al., 2009; Mathieu et al., 2008).

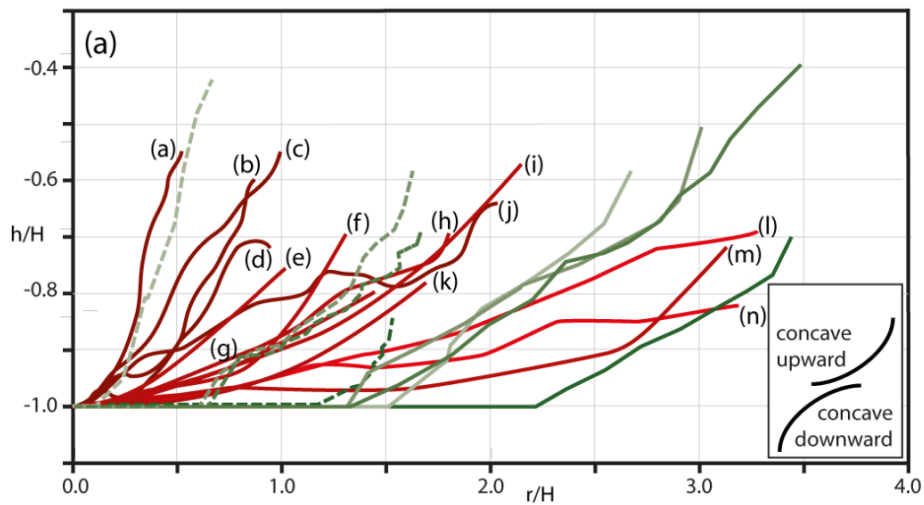
569 In comparison, our experimental saucer-shaped sills have outer sill inclination angles,  
570  $\theta_i = 15^\circ - 25^\circ$  and the inner to outer sill transition occurs when  $0.5 \leq r/H \leq 2.5$ , with no evidence  
571 for shear faulting in the LRD host material at the onset of inclined sheet formation. Therefore,  
572 the experiments reported here do not support a model of inelastic damage as a mechanical  
573 precursor for inclined sheet emplacement. Our experimental results are more compatible with  
574 LEFM models, in which saucer-shaped sills form as a consequence of asymmetrical stress  
575 fields generated by inflation of the inner flat sill and its elastic interaction with its surroundings  
576 and the free surface (Pollard and Holzhausen, 1979; Malthe-Sørenssen et al., 2004). This is  
577 supported by the sill profiles in Figure 5, which show that the outer inclined sills start to  
578 propagate upwards when  $r/H$  reaches values of 0.5 to 2.5. At this point, the sills climb upward  
579 with shallow inclinations (i.e.  $15^\circ \leq \theta_i \leq 25^\circ$ ) due to a change of the stress field, which is linked  
580 to the onset of overburden uplift.

#### 581 **4.4. Comparison of experimental and natural saucer-shaped sill profiles**

582 Vertical profiles of the experimental sills reported here are compared with natural  
583 saucer-shaped sill profiles in Figure 9a (modified after Walker and Gill, 2020) in which the  
584 intrusion height,  $h$ , and radius,  $r$ , are normalised by the overburden depth,  $H$ . The inner sill to  
585 inclined outer sheet transition in natural saucer-shaped sills occurs when  $r/H = 1$  to 4 (Fig 9a;  
586 Malthe-Sørenssen. et al., 2004; Galland et al., 2008) and the corresponding outer sill inclination  
587 angles,  $\theta_i = 10 - 30^\circ$ , are similar to our experimental results. Inclined outer sheets in nature  
588 typically initiate with a lower inclination angle that increases towards the surface, so they have  
589 concave upward profiles (Gill and Walker, 2020). Except for the Golden Valley and Tulipan  
590 Sills, which have  $r/H > 3.5$  (Fig. 2a), all of the normalised natural saucer-shaped sill profiles

591 plotted in Figure 9a share similar geometric features (i.e.,  $h/H$  and  $r/H$  ratios,  $\theta_i$  angles and  
 592 concave upward shapes) with our experimental results.

593



594

595

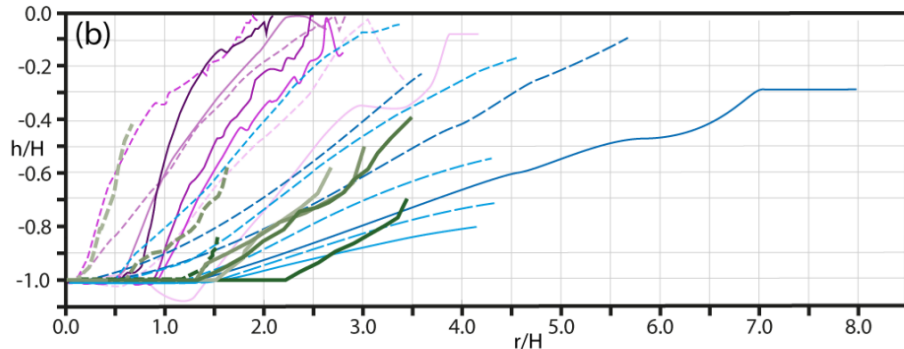
596

597

598

599

600

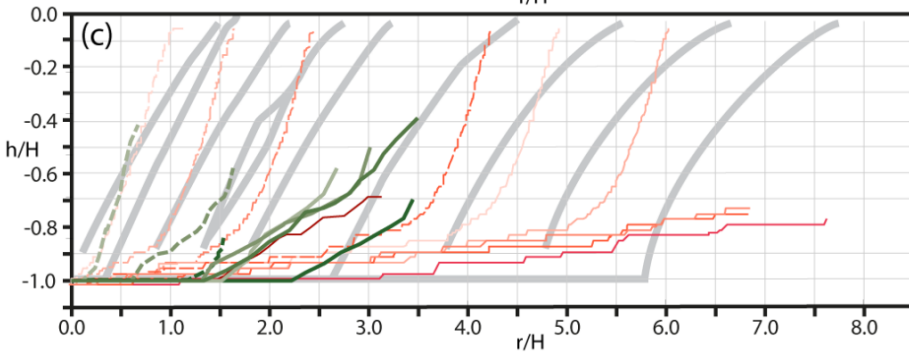


601

602

603

604



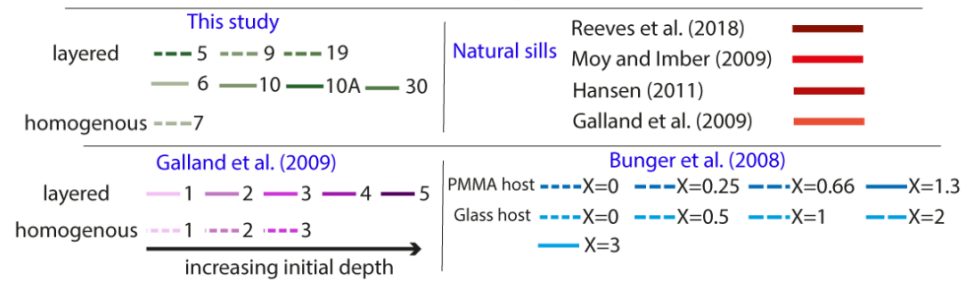
605

606

607

608

609

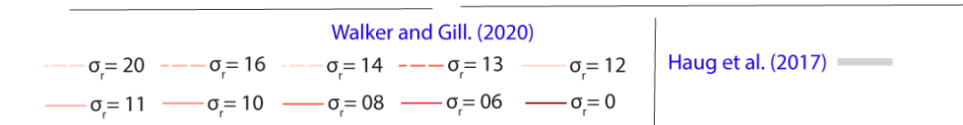


610

611

612

613



614

615 **Figure 9.** A comparison of normalised saucer-shaped sill profiles from this study with (a) nature, (b)  
616 laboratory experimental and (c) numerical models (modified after Walker and Gill, 2020). Except for  
617 the Golden Valley and Tulipan Sills (Fig. 2a), saucer-shaped sill profiles in this study are similar to  
618 natural examples with concave upward shapes (Fig. 9a). See fig. 2 for the details of the saucer-shaped  
619 sills in nature (fig. 9a; a – o).

620 The normalised profiles of saucer-shaped sills modelled in the laboratory by Bungler et  
621 al. (2008) and Galland et al. (2009) have steeper outer sill inclination angles with concave  
622 downward shapes in contrast to the experiments reported here (Fig. 9b). Bungler et al. (2008)  
623 used glass and polymethyl methacrylate (PMMA) as brittle-elastic host rock analogues and  
624 water, glycerine or glucose syrup as the magma analogue. They also introduced a  
625 dimensionless fracture toughness number,  $\chi = \frac{\sigma_r \sqrt{H}}{K_c}$  where  $K_c$  is the fracture toughness of the  
626 host material (Fig. 8b). In their experiments, the inner to outer sill transition occurs when  $0 \leq$   
627  $r/H \leq 2$ , increasing with increasing  $\chi$ -value (i.e., with increasing emplacement depth, horizontal  
628 compressive stress, or decreasing fracture toughness). Bungler et al.'s (2008) experimental sills  
629 have inclinations  $15^\circ < \theta_i < 30^\circ$ , which, except for their concave down profiles, is similar to  
630 both our model results and natural saucer-shaped sills (Fig. 9b).

631 Galland et al.'s (2009) laboratory experiments used elasto-plastic silica powder and  
632 vegetable oil as host rock and magma analogues, respectively (Fig. 9b). The injected oil formed  
633 cone sheets or vertical dykes within homogenous models whereas saucer-shaped intrusions  
634 formed in layered experiments. The inner to outer sill transition in their layered models occurs  
635 when  $r/H \sim 0.5 - 1.5$  with outer sill inclinations  $40^\circ < \theta_i < 50^\circ$ . However, these inclinations are  
636 steeper than those in nature and they also have strongly concave downward profiles.

637 In the numerical experiments by Haug et al. (2017), the inner-outer sill transition is  
638 prescribed by a fixed initial sill radius, which varied effectively from  $\sim 0.5$  to 6 km. In their  
639 models, the outer sheet inclinations ( $\theta_i$ ) adjacent to the inner sill are much steeper ( $\theta_i \geq 60^\circ$ )

640 than that those observed in this study and in nature, and they also have strongly concave  
641 downward profiles (Fig. 9c).

642         Recent numerical modelling by Gill and Walker (2020) and Walker and Gill (2020)  
643 used axisymmetric finite-element calculations to investigate how a compressive horizontal  
644 tectonic stress ( $\sigma_r$ ) changes the geometry and aspect ratio of saucer-shaped sills (Fig. 9c). Their  
645 model considered tensile fracture and shear failure crack tip separation mechanisms, and the  
646 input parameters were magma overpressure, host rock elasticity and the externally applied  
647 tectonic stress. In their analysis, when  $\sigma_r = 0$  MPa, the inner to outer transition occurs when  $r/H$   
648  $= 1.5$ ,  $\theta_i \sim 25^\circ$ , and the resulting outer sheet has a concave upward profile, in good agreement  
649 with our results. Walker and Gill (2020) showed that as  $\sigma_r$  increases ( $0 \text{ MPa} \leq \sigma_r \leq 5 \text{ MPa}$ ),  
650 saucer-shaped sills form with increasingly wider inner sills ( $1.5 \leq r/H \leq 4.5$ ) and shallower  
651 outer sill inclinations ( $25^\circ < \theta_i < 1^\circ$ ). However, for  $5 \text{ MPa} \leq \sigma_r \leq 10 \text{ MPa}$ ,  $\theta_i$  is constant at  $1^\circ$   
652 and  $r/H$  reduces to 0.5 from 4.5 (Fig. 4 in Walker and Gill, 2020). Furthermore, they concluded  
653 that the model results for  $5 \text{ MPa} \leq \sigma_r \leq 10 \text{ MPa}$  show a good fit to natural saucer-shaped sills,  
654 and that the sill tips propagate by Mode I tensile failure. However, when  $\sigma_r > 10 \text{ MPa}$ ,  $r/H <$   
655  $0.5$  and  $\theta_i$  increases up to  $45^\circ$ , and sill tips propagate by host rock shear failure (Fig. 8c).

656         In many of the laboratory (Bunger et al., 2008; Galland et al., 2009) and numerical  
657 simulations (Haug et al., 2017) reviewed above, the resulting saucer-shaped sills have concave  
658 downward inclined outer sheets with steep inclination angles. This contrasts with inclined outer  
659 sheets in most natural examples, which are concave upward with shallow inclination angles  
660 (Walker and Gill, 2020) (Fig. 9a). Numerical simulations by Gill and Walker (2020) and  
661 Walker and Gill (2020) show that a strong compressive stress regime is required to match the  
662 geometry of natural saucer-shaped sills. However, the  $h/H$  and  $r/H$  ratios, outer sheet  
663 inclination angles and concave upward shapes observed in our experiments closely match the  
664 geometries of natural saucer-shaped sills, without the imposition of a horizontal tectonic stress.

665 Therefore, the experiments presented here highlight the importance of host-rock rheology (i.e.,  
666 visco-elastic-plastic) for saucer-shaped sill formation, in addition to the possible contribution  
667 of horizontal stress boundary conditions.

## 668 **5. Conclusions**

669 We have described the results of laboratory modelling of saucer-shaped sill intrusions,  
670 in which paraffin oil (magma analogue) was injected at a constant volumetric flow rate into a  
671 homogenous or two-layer model crust made of visco-elastic-plastic Laponite RD<sup>®</sup> (LRD) gel.  
672 The resulting experimental saucer-shaped sills form by the interaction between the outwardly  
673 propagating and vertically inflating sill and the overburden its overlying free surface. Our main  
674 findings are:

- 675 1. Saucer-shaped sills emplaced into homogenous LRD have the shortest inner sill diameter, a  
676 smooth transition into inclined sheet and steeply inclined outer sill compared to two-layer  
677 experiments.
- 678 2. In two-layer experiments, saucer-shaped sills develop with a flat-lying inner sill that  
679 followed the L1/L2 interface and an inclined outer sheet that propagates through the upper  
680 layer towards the model surface. The inner sill to inclined outer sheet transition is sharp and  
681 occurs over a range of inner sill radius to overburden depth ( $r/H$ ) ratios between 0.5 and 2,  
682 which increase with decreasing Young's modulus or rigidity ratio ( $E_r$ ) and increasing  
683 volumetric injection rate.
- 684 3. The horizontal growth rate of all saucer-shaped sill intrusions is uniform for all values of  $E_r$   
685 and a constant volumetric flux rate ( $Q_i = 1 \text{ ml/min}$ ). However, for the same  $E_r$ , the growth rate  
686 increases when  $Q_i$  is increased (Exp 10A;  $Q_i = 5 \text{ ml/min}$ ).
- 687 4. The saucer-shaped sills that formed in our experiments are compatible with brittle-elastic  
688 (LEFM) models in which the inner sill to outer inclined sheet transition occurs due to an  
689 elasticity-dominated interaction between the growing inner sill and the surrounding material

690 and free surface. However, as discussed by Arachchige et al. (in review), marginal lobes and  
691 finger-like segments observed in most experiments are more likely linked to small-scale visco-  
692 plastic instabilities occurring at the tip of the propagating sills. This suggests the operation of  
693 scale-dependent deformation processes, with brittle-elastic (LEFM) processes dominating at  
694 the whole of intrusion scale and visco-plastic processes dominating at the crack tip scale.

695 5. Experiments suggest that there is no strict requirement of high horizontal stresses to form  
696 natural saucer-shaped sill geometries and show the importance of host rock rheology of making  
697 complex sill geometries.

## 698 **Acknowledgements**

699 We gratefully acknowledge support from an Australian Research Council Discovery  
700 Grant (DP190102422) to A.R.C. and a DIPRS PhD scholarship from Monash University  
701 (Melbourne) to U.S.N.A.

## 702 **References**

- 703 Arachchige, U.N., Cruden, A.R., Weinberg, R., 2021. Laponite gels - visco-elasto-plastic  
704 analogues for geological laboratory modelling. *Tectonophysics* 805, 228773.  
705 <https://doi.org/10.1016/j.tecto.2021.228773>
- 706 Barnett, Z.A., Gudmundsson, A., 2014. Numerical modelling of dykes de fl ected into sills to  
707 form a magma chamber. *Journal of Volcanology and Geothermal Research* 281, 1–11.  
708 <https://doi.org/10.1016/j.jvolgeores.2014.05.018>
- 709 Bertelsen, H.S., Rogers, B.D., Galland, O., Dumazer, G., Abbana Benanni, A., 2018.  
710 Laboratory Modeling of Coeval Brittle and Ductile Deformation During Magma  
711 Emplacement Into Viscoelastic Rocks. *Frontiers in Earth Science* 6.  
712 <https://doi.org/10.3389/feart.2018.00199>
- 713 Bonn, D., Tanase, S., Abou, B., Tanaka, H., Meunier, J., 2002. Laponite: Aging and shear  
714 rejuvenation of a colloidal glass. *Physical Review Letters* 89, 157011–157014.

715 <https://doi.org/10.1103/PhysRevLett.89.015701>

716 Bunger, A.P., Detournay, E., 2005. Asymptotic solution for a penny-shaped near-surface  
717 hydraulic fracture. *Engineering Fracture Mechanics* 72, 2468–2486.  
718 <https://doi.org/10.1016/j.engfracmech.2005.03.005>

719 Bunger, A.P., Detournay, E., Jeffrey, R.G., 2005. Étude Expérimentale Du Comportement En  
720 Bout D’Une Fracture Hydraulique Se Propageant Près D’Une Surface Libre. *Comptes*  
721 *Rendus - Mécanique* 333, 299–304. <https://doi.org/10.1016/j.crme.2005.01.004>

722 Bunger, A.P., Jeffrey, R.G., Detournay, E., 2008. Evolution and morphology of saucer-shaped  
723 sills in analogue experiments. *Geological Society Special Publication* 302, 109–120.  
724 <https://doi.org/10.1144/SP302.8>

725 Chanceaux, L., Menand, T., 2016. The effects of solidification on sill propagation dynamics  
726 and morphology. *Earth and Planetary Science Letters* 442, 39–50.  
727 <https://doi.org/10.1016/j.epsl.2016.02.044>

728 Chevallier, L., Woodford, A., 1999. Morpho-tectonics and mechanism of emplacement of the  
729 dolerite rings and sills of the western Karoo, South Africa. *South African Journal of*  
730 *Geology* 102, 43–54.

731 Cruden et al, 2017. Geometric Scaling of Tabular Igneous Intrusions: Implications for  
732 Emplacement and Growth. *Advances in Volcanology* 1–4. <https://doi.org/10.1007/11157>

733 Eide, C.H., Schofield, N., Jerram, D.A., Howell, J.A., 2017. Basin-scale architecture of deeply  
734 emplaced sill complexes: Jameson Land, East Greenland Christian. *Journal of the*  
735 *Geological Society* 174, 23–40. <https://doi.org/10.1144/jgs2016-018>

736 Fialko, Y., Khazan, Y., Simons, M., 2001. Deformation due to a pressurized horizontal circular  
737 crack in an elastic half-space, with applications to volcano geodesy. *Geophysical Journal*  
738 *International* 146, 181–190. <https://doi.org/10.1046/j.1365-246X.2001.00452.x>

739 Galland, O., Planke, S., Neumann, E.R., Malthe-Sørenssen, A., 2009. Experimental modelling

740 of shallow magma emplacement: Application to saucer-shaped intrusions. *Earth and*  
741 *Planetary Science Letters* 277, 373–383. <https://doi.org/10.1016/j.epsl.2008.11.003>

742 Gill, S.P.A., Walker, R.J., 2020. The Roles of Elastic Properties, Magmatic Pressure, and  
743 Tectonic Stress in Saucer-Shaped Sill Growth. *Journal of Geophysical Research: Solid*  
744 *Earth* 125, 1–24. <https://doi.org/10.1029/2019jb019041>

745 Hansen, D.M., Cartwright, J., 2006. Saucer-shaped sill with lobate morphology revealed by 3D  
746 seismic data: implications for resolving a shallow-level sill emplacement mechanism.  
747 *Journal of the Geological Society* 163, 509–523. [https://doi.org/10.1144/0016-764905-](https://doi.org/10.1144/0016-764905-073)  
748 073

749 Hansen, J., 2015. A numerical approach to sill emplacement in isotropic media: Do saucer-  
750 shaped sills represent “natural” intrusive tendencies in the shallow crust? *Tectonophysics*  
751 664, 125–138. <https://doi.org/10.1016/j.tecto.2015.09.006>

752 Haug, Ø.T., Galland, O., Souloumiac, P., Souche, A., Guldstrand, F., Schmiedel, T., 2017.  
753 Inelastic damage as a mechanical precursor for the emplacement of saucer-shaped  
754 intrusions. *Geology* 45, 1099–1102. <https://doi.org/10.1130/G39361.1>

755 Hutton, D.H.W., 2009. Insights into magmatism in volcanic margins: bridge structures and a  
756 new mechanism of basic sill emplacement - Theron Mountains, Antarctica. *Petroleum*  
757 *Geoscience* 15, 269–278. <https://doi.org/10.1144/1354-079309-841>

758 Kaushal, M., Joshi, Y.M., 2014. Linear viscoelasticity of soft glassy materials. *Soft Matter* 10,  
759 1891–1894. <https://doi.org/10.1039/c3sm52978a>

760 Kavanagh, J.L., Boutelier, D., Cruden, A.R., 2015. The mechanics of sill inception,  
761 propagation and growth: Experimental evidence for rapid reduction in magmatic  
762 overpressure. *Earth and Planetary Science Letters* 421, 117–128.  
763 <https://doi.org/10.1016/j.epsl.2015.03.038>

764 Kavanagh, J.L., Burns, A.J., Hilmi Hazim, S., Hignett, S., Wood, E.P., Martin, S.A., Dennis,

765 D.J.C.C., 2018. Challenging dyke ascent models using novel laboratory experiments:  
766 Implications for reinterpreting evidence of magma ascent and volcanism. *Journal of*  
767 *Volcanology and Geothermal Research* 354, 87–101.  
768 <https://doi.org/10.1016/j.jvolgeores.2018.01.002>

769 Kavanagh, J.L., Menand, T., Daniels, K.A., 2013. Gelatine as a crustal analogue: Determining  
770 elastic properties for modelling magmatic intrusions. *Tectonophysics* 582, 101–111.  
771 <https://doi.org/10.1016/j.tecto.2012.09.032>

772 Kavanagh, J.L., Menand, T., Sparks, R.S.J., 2006. An experimental investigation of sill  
773 formation and propagation in layered elastic media. *Earth and Planetary Science Letters*  
774 245, 799–813. <https://doi.org/10.1016/j.epsl.2006.03.025>

775 Lister, J.R., Kerr, R.C., 1991. Fluid-mechanical models of crack propagation and their  
776 application to magma transport in dykes. *Journal of Geophysical Research* 96, 10049.  
777 <https://doi.org/10.1029/91JB00600>

778 Magee, C., Muirhead, J.D., Karvelas, A., Holford, S.P., Jackson, C.A.L., Bastow, I.D.,  
779 Schofield, N., Stevenson, C.T.E., McLean, C., McCarthy, W., Shtukert, O., 2016. Lateral  
780 magma flow in mafic sill complexes. *Geosphere* 12, 809–841.  
781 <https://doi.org/10.1130/GES01256.1>

782 Malthe-Sørenssen, Planke, A., Svensen, S.H., Jamtveit, B., 2004. Formation of saucer-shaped  
783 sills. *Geological Society, London, Special Publications* 234, 215–227.

784 Mathieu, L., van Wyk de Vries, B., Holohan, E.P., Troll, V.R., 2008. Dykes, cups, saucers and  
785 sills: Analogue experiments on magma intrusion into brittle rocks. *Earth and Planetary*  
786 *Science Letters* 271, 1–13. <https://doi.org/10.1016/j.epsl.2008.02.020>

787 Moy, D.J., Imber, J., 2009. A critical analysis of the structure and tectonic significance of rift-  
788 oblique lineaments ('transfer zones') in the Mesozoic-Cenozoic succession of the Faroe-  
789 Shetland basin, NE Atlantic margin. *Journal of the Geological Society* 166, 831–844.

790 <https://doi.org/10.1144/0016-76492009-010>

791 Norris, J., Giese, R.F., Costanzo, P.M., Vanoss, C.J., 1993. The Surface Energies of Cation  
792 Substituted Laponite. Clay Minerals 28, 1–11.  
793 <https://doi.org/10.1180/claymin.1993.028.1.01>

794 Persikov, E.S., 1991. The Viscosity of Magmatic Liquids: Experiment, Generalized Patterns.  
795 A Model for Calculation and Prediction. Applications. 1–40. [https://doi.org/10.1007/978-](https://doi.org/10.1007/978-1-4612-3128-8_1)  
796 [1-4612-3128-8\\_1](https://doi.org/10.1007/978-1-4612-3128-8_1)

797 Pollard, D.D., Holzhausen, G., 1979. On the mechanical interaction between a fluid-filled  
798 fracture and the earth's surface. Tectonophysics 53, 27–57. [https://doi.org/10.1016/0040-](https://doi.org/10.1016/0040-1951(79)90353-6)  
799 [1951\(79\)90353-6](https://doi.org/10.1016/0040-1951(79)90353-6)

800 Pollard, D.D., Johnson, A.M., 1973. Mechanics of growth of some laccolithic intrusions in the  
801 Henry mountains, Utah, II. Bending and failure of overburden layers and sill formation.  
802 Tectonophysics 18, 311–354. [https://doi.org/10.1016/0040-1951\(73\)90051-6](https://doi.org/10.1016/0040-1951(73)90051-6)

803 Pollard, D.D., Muller, O.H., Dockstader, D.R., 1975. The form and growth of fingered sheet  
804 intrusions. Bulletin of the Geological Society of America 86, 351–363.  
805 [https://doi.org/10.1130/0016-7606\(1975\)86<351:TFAGOF>2.0.CO;2](https://doi.org/10.1130/0016-7606(1975)86<351:TFAGOF>2.0.CO;2)

806 Polteau, S., Mazzini, A., Galland, O., Planke, S., Malthe-Sørensen, A., 2008. Saucer-shaped  
807 intrusions: Occurrences, emplacement and implications. Earth and Planetary Science  
808 Letters 266, 195–204. <https://doi.org/10.1016/j.epsl.2007.11.015>

809 Ranalli, G., 2001. Experimental tectonics: From Sir James Hall to the present. Journal of  
810 Geodynamics 32, 65–76. [https://doi.org/10.1016/S0264-3707\(01\)00023-0](https://doi.org/10.1016/S0264-3707(01)00023-0)

811 Reeves, J., Magee, C., Jackson, C.A.L., 2018. Unravelling intrusion-induced forced fold kine-  
812 matics and ground deformation using 3D seismic reflection data.  
813 <https://doi.org/https://doi.org/10.30909/vol.01.01.0117>

814 Rivalta, E., B, M., Dahm, T., 2005. Buoyancy-driven fracture ascent : Experiments in layered

815           gelatine. 144, 273–285. <https://doi.org/10.1016/j.jvolgeores.2004.11.030>

816 Rubin, A.M., 1995. Propagation of magma-filled cracks. *Annu. Rev. Earth Planet. Sci* 287–  
817           336.

818 Ruzicka, B., Zaccarelli, E., 2011. A fresh look at the Laponite phase diagram. *Soft Matter* 7,  
819           1268–1286. <https://doi.org/10.1039/c0sm00590h>

820 Spacapan, J.B., Galland, O., Leanza, H.A., Planke, S., 2017. Igneous sill and finger  
821           emplacement mechanism in shale-dominated formation: a field study at Cuesta del  
822           Chihuido, Neuquén Basin, Argentina. *Journal of the Geological Society* 174, 422–433.  
823           <https://doi.org/10.1144/jgs2016-056>

824 Spence, D.A., Turcotte, D.L., 1985. Magma-driven propagation of cracks. *Journal of*  
825           *Geophysical Research* 90, 575–580.

826 Thomson, K., Hutton, D., 2004. Geometry and growth of sill complexes: Insights using 3D  
827           seismic from the North Rockall Trough. *Bulletin of Volcanology* 66, 364–375.  
828           <https://doi.org/10.1007/s00445-003-0320-z>

829 Walker, R.J., Gill, S.P.A., 2020. Tectonic stress controls saucer-shaped sill geometry and  
830           emplacement mechanism. *Geology* 48, 898–902. <https://doi.org/10.1130/G47604.1>

831